Highly-sensitive gas pressure sensor using twin-core fiber based in-line Mach-Zehnder interferometer

Zhengyong Li,[1] Changrui Liao,[1] Yiping Wang,[1,*] Lei Xu,[2] Dongning Wang,[3] Xiaopeng Dong,[4] Shen Liu,[1] Qiao Wang,[1] Kaiming Yang,[1] and Jiangtao Zhou[1]

[1]*Key Laboratory of Optoelectronic Devices and Systems of Ministry of Education and Guangdong Province, College of Optoelectronic Engineering, Shenzhen University, Shenzhen 518060, China*
[2]*Department of Computing, The HongKong Polytechnic University, HongKong, China*
[3]*Department of Electrical Engineering, The Hong Kong Polytechnic University, Hong Kong, China*
[4]*School of Information Science and Engineering, Xiamen University, Xiamen 361005, China*
*ypwang@szu.edu.cn

Abstract: A Mach-Zehnder interferometer based on a twin-core fiber was proposed and experimentally demonstrated for gas pressure measurements. The in-line Mach-Zehnder interferometer was fabricated by splicing a short section of twin-core fiber between two single mode fibers. A micro-channel was created to form an interferometer arm by use of a femtosecond laser to drill through one core of the twin-core fiber. The other core of the fiber was remained as the reference arm. Such a Mach-Zehnder interferometer exhibited a high gas pressure sensitivity of −9.6 nm/MPa and a low temperature cross-sensitivity of 4.4 KPa/°C. Moreover, ultra-compact device size and all-fiber configuration make it very suitable for highly-sensitive gas pressure sensing in harsh environments.

References and links

1. Z. Li, Y. Wang, C. Liao, S. Liu, J. Zhou, X. Zhong, Y. Liu, K. Yang, Q. Wang, and G. Yin, "Temperature-insensitive refractive index sensor based on in-fiber Michelson interferometer," Sens. Actuators B Chem. **199**(0), 31–35 (2014).
2. G. L. Yin, S. Q. Lou, W. L. Lu, and X. Wang, "A high-sensitive fiber curvature sensor using twin core fiber-based filter," Appl. Phys. B **115**(1), 99–104 (2014).
3. Y. P. Wang, J. P. Chen, and Y. J. Rao, "Torsion characteristics of long-period gratings induced by high-frequency CO2 laser pulses," J. Opt. Soc. Am. B **22**(6), 1167–1172 (2005).
4. Y. Wang, "Review of long period fiber gratings written by CO2 laser," J. Appl. Phys. **108**(8), 081101 (2010).
5. C. R. Liao, D. N. Wang, M. Wang, and M. H. Yang, "Fiber in-line Michelson Interferometer Tip Sensor Fabricated by Femtosecond Laser," IEEE Photon. Technol. Lett. **24**(22), 2060–2063 (2012).
6. C. R. Liao, Y. Li, D. N. Wang, T. Sun, and K. T. V. Grattan, "Morphology and thermal stability of fiber Bragg gratings for sensor applications written in H2-free and H2-loaded fibers by Femtosecond laser," IEEE Sens. J. **10**(11), 1675–1681 (2010).
7. Z. Qi, L. Nan, T. Fink, L. Hong, P. Wei, and H. Ming, "Fiber-optic pressure sensor based on π-phase-shifted fiber Bragg grating on side-hole fiber," IEEE Photon. Technol. Lett. **24**(17), 1519–1522 (2012).
8. G. Hu and D. Chen, "Side-hole dual-core photonic crystal fiber for hydrostatic pressure sensing," J. Lightwave Technol. **30**(14), 2382–2387 (2012).
9. T. Martynkien, P. Mergo, and W. Urbanczyk, "Sensitivity of birefringent microstructured polymer optical fiber to hydrostatic pressure," J. Lightwave Technol. **25**(16), 1562–1565 (2013).
10. J. Long, G. Bai-Ou, and W. Huifeng, "Sensitivity characteristics of Fabry-Perot pressure sensors based on hollow-core microstructured fibers," J. Lightwave Technol. **31**(15), 2526–2532 (2013).
11. M. Jun, J. Jian, J. Long, and J. Wei, "A compact fiber-tip micro-cavity sensor for high-pressure measurement," IEEE Photon. Technol. Lett. **23**(21), 1561–1563 (2011).
12. C. Liao, S. Liu, L. Xu, C. Wang, Y. Wang, Z. Li, Q. Wang, and D. N. Wang, "Sub-micron silica diaphragm-based fiber-tip Fabry-Perot interferometer for pressure measurement," Opt. Lett. **39**(10), 2827–2830 (2014).
13. J. Ma, W. Jin, H. L. Ho, and J. Y. Dai, "High-sensitivity fiber-tip pressure sensor with graphene diaphragm,"

Opt. Lett. **37**(13), 2493–2495 (2012).

14. F. Xu, D. Ren, X. Shi, C. Li, W. Lu, L. Lu, L. Lu, and B. Yu, "High-sensitivity Fabry-Perot interferometric pressure sensor based on a nanothick silver diaphragm," Opt. Lett. **37**(2), 133–135 (2012).

15. J. C. Xu, X. W. Wang, K. L. Cooper, and A. B. Wang, "Miniature all-silica fiber optic pressure and acoustic sensors," Opt. Lett. **30**(24), 3269–3271 (2005).

16. Y. Wang, M. Yang, D. N. Wang, S. Liu, and P. Lu, "Fiber in-line Mach-Zehnder interferometer fabricated by femtosecond laser micromachining for refractive index measurement with high sensitivity," J. Opt. Soc. Am. B **27**(3), 370–374 (2010).

17. D. Duan, Y. Rao, and T. Zhu, "High sensitivity gas refractometer based on all-fiber open-cavity Fabry-Perot interferometer formed by large lateral offset splicing," J. Opt. Soc. Am. B **29**(5), 912–915 (2012).

18. M. Deng, C. P. Tang, T. Zhu, Y. J. Rao, L. C. Xu, and M. Han, "Refractive index measurement using photonic crystal fiber-based Fabry-Perot interferometer," Appl. Opt. **49**(9), 1593–1598 (2010).

1. Introduction

Fiber optic sensors have been demonstrated to extremely attractive for various areas of biomedicine, automotive industries and environmental monitoring [1–6]. Among them, optical fiber pressure sensors are of great interests owing to their great multiplexing capability, compact size, immunity to electromagnetic interference and easy signal detection. So far, various optical fiber configurations for pressure measurement have been reported, i.e. π-phase-shift fiber Bragg grating fabricated on side-hole fiber [7], side-hole dual-core photonic crystal fiber [8], and PMMA birefringent fiber [9]. Fabry–Pérot interferometers (FPIs) have played an extra-ordinary role in pressure sensing due to their compact size and easy fabrication [10–15]. Hollow-core fiber based FPI exhibits an pressure sensitivity of −23.4 pm/MPa [10]. Fiber-tip micro-bubble based FPI shows a pressure sensitivity of 315 pm/MPa [11]. Liao et al. optimized the fabrication process and enhanced the pressure sensitivity up to 1036 pm/MPa [12]. All silica structure of the above FPIs limits the pressure performance and in order to further improve the pressure sensitivity, new FPIs based on grapheme diaphragm [13] and silver diaphragm [14] have been realized and exhibited an ultrahigh pressure sensitivity of 39.4 nm/kPa and 70.5 nm/kPa, respectively. Unfortunately, the mechanical strength of these FPIs is poor because the thin diaphragm attached at the fiber end is easily cracked that will limit its application in high pressure environment.

In this letter, we present a highly-sensitive pressure sensor based on a fiber in-line MZI, which is fabricated by using femtosecond laser (FS) micromachining and fusion splicing technique. This fiber interferometer is constructed by splicing a short section of twin-core fiber (TCF) between two single mode fibers (SMFs) and the separate cores of the TCF perform as the two interference arms. One arm contains a micro-channel, which is created by removing part of one core of the TCF, and the second arm is the other complete core. Different from previously reported fiber pressure sensors, gas density change in the micro-channel induced by the increased pressure causes the spectral response. The TCF-based MZI exhibits a high pressure sensitivity of −9.6 nm/MPa within the pressure range between 0 and 2 MPa and a small cross-sensitivity to temperature of 4.4 KPa/°C. Moreover, the ultra-compact size of the fiber interferometer is able to ensure a precise sensing location.

2. Operating principle and fabrication

Figure 1 is shown the schematic diagram of the proposed TCF-based MZI. A short section of TCF is spliced between two sections of SMFs and a micro-channel is created in the $core_2$ of the TCF by using FS laser micromachining. The light propagating in SMF_1 is equally splitted into two beams in the TCF, which is denoted as I_{in1} and I_{in2}, respectively. The length of TCF is very short so that the mode coupling effect between the two cores can be neglected, that is to say, the light of two cores is able to propagate independently. Beam (I_{in1}) remains to propagate in the $core_1$ while beam (I_{in2}) travels through the micro-channel, where an optical path difference (OPD) is obtained. When the two output beams, i.e. I_{out1} and I_{out2} corresponding to I_{in1} and I_{in2}, recombined in SMF_2, the notable interference spectrum is

achieved because of the phase difference between the two output beams. The output intensity of TCF-based MZI can be expressed as,

$$I = I_{out1} + I_{out2} + 2\sqrt{I_{out1}I_{out2}}\cos(\frac{2\pi L\Delta n}{\lambda} + \varphi_0),\qquad(1)$$

where λ is the light wavelength, L is the length of the micro-channel, $\Delta n = n_{core}-n_{channel}$ is the effective RI difference between the two interference arms, where n_{core} and $n_{channel}$ are the effective RI of the core mode and the channel mode, and φ_0 is the initial phase of the interference. According to Eq. (1), the interference signal reaches the minimum value when the following condition is satisfied,

$$\frac{2\pi L\Delta n}{\lambda_m} + \varphi_0 = (2m+1)\pi,\qquad(2)$$

where m is an integer, λ_m is the wavelength of the mth order interference dip.
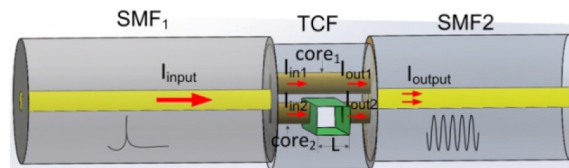

Fig. 1. Schematic diagram of the TCF based MZI.

The fabrication process of the proposed TCF-based MZI involves of two steps. The first step: one end of the TCF was spliced with an SMF (Corning, SMF-28) with the core/cladding diameters of 8/125 μm by using a commercial fusion splicer (Fujikura FSM-60s). The cross-sectional morphology of the TCF that is supplied by Xiamen University is shown in Fig. 2(c), where the cladding diameter is 125 μm and the major/mirror axes of the two elliptical cores are measured to be ~10.9 and ~6.5μm, respectively. The splicing process is demonstrated in Fig. 2, where a red laser beam was launched into the SMF$_1$ and the light intensity of the two TCF cores was observed by using an optical microscope. The offset distance between the SMF and the TCF was carefully adjusted to let the light intensity in the two cores become roughly equal. Figures 2(a) and 2(b) shows the unequal and equal splitting ratios when different offsets are employed. In the experiment the TCF with a length of ~200μm was used and the other end of TCF was spliced with another SMF with an optimized offset value to obtain the maximum intensity output. Splicing errors, i.e. fiber offset distance in splicing, will result in the decay of the fringe visibility that is harmful to sensing applications and a very short piece of TCF (~200μm) was employed in this MZI to avoid the light coupling between the two cores and decrease the total insertion loss of this device.
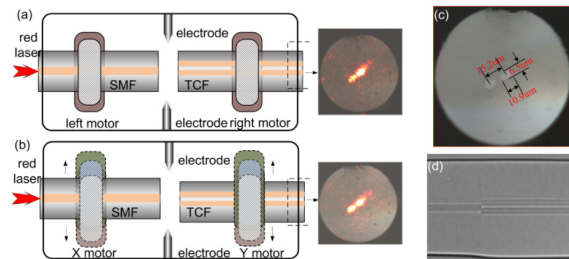

Fig. 2. Schematic diagram of the splicing process assisted with a red beam irradiation, (a) before fusion splicing; (b) adjusting X and Y motors to make the light intensity of the two cores become equal with each other; (c) microscope image of the cross section of TCF; and (d) microscope image of the spliced joint.

The second step: a micro-channel was drilled through the first core, i.e. $core_1$, of the TCF by employing a FS laser (Spectra-Physics Solstice, 120 fs, 800 nm, 1 KHz, 4 mJ), as described below. The laser beam was focused by use of an objective lens with an NA value of 0.25. The laser power was adjustable in the range between 0 and 4mJ by rotating a half-wave plate followed by a polarizer, and the average on-target laser power was maintained at ~20mW. The TCF was mounted on a computer-controlled X-Y-Z translation stage (Newport)with a resolution of 10 nm. The fabrication of the micro-channel was similar to the process described in Ref [16]. Firstly, FS laser beam was focused on the center of the fiber core and shifted by 15 μm away from fiber axis. This position was set to be the jumping-off point. Secondly, the focused FS laser beam was scanned with a distance of 45μm along the fiber axis at a speed of 5 μm/s, and then was returned to the jumping-off point. Such a process is called one scanning cycle. Thirdly, the laser beam was moved toward the core with a step of 5μm in order to start next scanning cycle. The laser was switched off as soon as an expected transmission spectrum was observed. Thus a micro-channel was created in the TCF, as shown in Figs. 3(a) and 3(b). Finally, the achieved micro-channel was cleaned by using alcohol to remove silica scraps. The size and geometry of the micro-channel is very important for the spectral property of our fiber MZI, i.e. insertion loss, fringe spectrum range and fringe visibility. Thanks to the ultra-small focal point of the FS laser beam and the nano-positioning stages employed, the size and geometry of the micro-channel can be well guaranteed in our experiment.
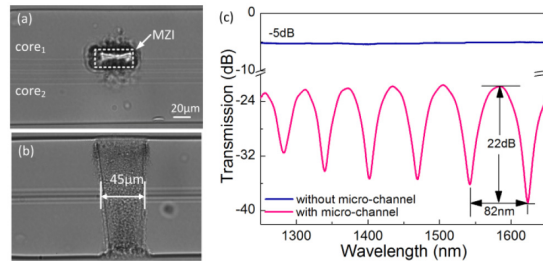

Fig. 3. (a) Top-view and (b) side-view microscope images of the created micro-channel; (c) transmission spectra of the TCF with and without a micro-channel in air.
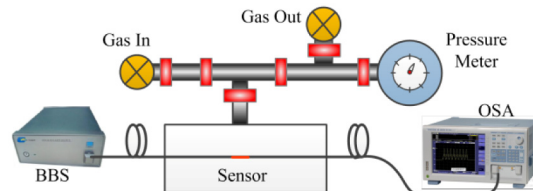

Fig. 4. Experimental setup for gas pressure measurements.

The transmission spectrum was measured in real time by using a broadband light source (BBS, Fiberlaker) ranging from 1250 to 1670 nm and an optical spectrum analyzer (OSA, Yokogama, AQ6370C). Figure 3(c) shows the transmission spectra of the device before and after the micro-channel was drilled in the TCF in air. Before drilling of the micro-channel, the initial insertion loss is ~5 dB, which mainly comes from the splicing loss between the SMF and TCF. The flat spectrum indicates that there is no OPD induced by the TCF being spliced between two SMFs. After drilling the micro-channel with a length of 50 μm, the insertion loss is increased to ~21dB and the fringe visibility of ~22 dB and the fringe spectral range (FSR) of ~82 nm are obtained. One core of TCF was removed so that the effective RI of this arm is reduced to 1.0 (air) but another arm is unchanged (silica). Thus, a significant OPD can be achieved. The fringe visibility depends on the intensity of I_{out1} and I_{out2}. The first splicing joint

between SMF$_1$ and TCF equally splits the input light (I$_{in1}$≈I$_{in2}$). The appearance of the micro-channel brings a large insertion loss to I$_{in2}$, which changes the balance between I$_{out1}$ and I$_{out2}$. So a poor fringe visibility is obtained.

3. Gas pressure and temperature experiments

The gas pressure response of the TCF-based MZI is tested and the experimental setup is shown in Fig. 4, where a BBS and an OSA with a resolution of 0.05 nm are employed to measure the transmission spectrum. The device is placed into the gas chamber, where a commercial gas pressure generator with a stability of ± 0.2 KPa is equipped with a high-precision digital pressure meter (ConST-811) to measure the pressure in the chamber. The chamber is fitted with a feed-through and sealed by strong glue to extend the fiber pigtail outside the chamber for real-time measurement. The pressure in the chamber is increased from 0 to 2 MPa with an interval of 0.2 MPa at room temperature, remaining at each step for 5 min.
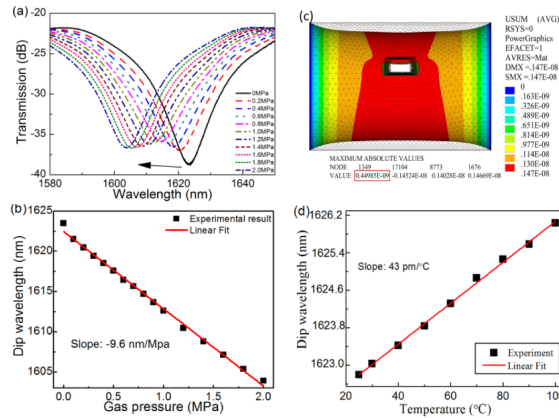

Fig. 5. (a) Transmission spectral evolution within the wavelength range from 1580 to 1650nm when the gas pressure increases from 0 to 2 MPa; (b) dip wavelength versus gas pressure; (c) Simulation model of the micro-channel deformation; (d) dip wavelength versus temperature.

Figure 5(a) shows the transmission spectra of the TCF-based MZI in different air pressure conditions and it can be found that the fringe dip shifts toward shorter wavelength with the applied pressure. The relationship between the wavelength of the fringe dip and the pressure is illustrated in Fig. 5(b), where a good linear response with an ultra-high pressure sensitivity of −9.6 nm/MPa is obtained. When the OSA was working with a resolution of 0.05 nm, the minimum detectable pressure changecan be calclulated to be ~5.2 KPa.

Firstly, it is important to discuss the deformation of the micro-channel with the increased gas pressure. A longitudinal strain (ε) translated from the lateral pressure P through Poisson's ratio is [17]

$$\varepsilon = \frac{\Delta L}{L} = \frac{(1-2\delta)}{E}P, \tag{3}$$

where E is the Young's modulus, δ is the Poisson's ratio, L is the micro-channel length, and P is the applied gas pressure. Assuming E = 73 GPa, δ = 0.17, L = 50 μm, and P = 1 MPa, the value of ε and the length change of micro-channel ΔL are calculated to be 9.04×10^{-6} and 0.452 nm, respectively. Simulation model is also established in ANSYS with the same parameters setting as above. The simulation result under the applied pressure of 1MPa is displayed in Fig. 5(c) and it can be seen from this figure that the length of the micro-channel is increased by 0.449 nm, which agrees well with the calculated result. From Eqs. (2) and (3), the relationship between the longitudinal strain of the interferometer cavity and the induced

dip wavelength shift can be expressed as $\varepsilon = \Delta L/L = \Delta\lambda/\lambda$. The applied gas pressure of 1 MPa will result in a very small dip movement of 14 pm, which could be ignored.

Assuming that the length of micro-channel is a constant, the pressure sensitivity can be derived from Eq. (2) as

$$\frac{d\lambda}{dP} = \frac{\lambda}{\Delta n}\frac{d(\Delta n)}{dP}, \qquad\qquad (4)$$

where d(Δn)/dP illustrates the RI change of air in micro-channel varying with pressure. At room temperature (15~25 °C), the RI of air is a function of the pressure and temperature [18]:

$$n = 1 + \frac{2.8793\times10^{-9}\times P}{1+0.003671\times t}, \qquad\qquad (5)$$

where n, P, t are the RI of air, the pressure (Pa), and the temperature (°C). If the temperature remains unchanged, there is a linear relationship between the air RI and the pressure. d(Δn)/dP can be calculated to be 2.63×10^{-3} when the temperature is 25 °C and the pressure is increased to 2 MPa. From Eq. (4) the pressure sensitivity of the TCF-based MZI can be calculated to be ~9.52 nm/MPa at 1610 nm for Δn = 1.445-1.0 = 0.445, which is very close to the experimental result. Therefore, the RI variation of the air in the micro-channel induced by the increased pressure plays a leading role on its pressure response. Comparing with the previously reported fiber pressure sensors, such as π-phase-shifted FBG (6.9 pm/Mpa) [7], side-hole dual-core photonic crystal fiber (32 pm/Mpa) [8], fiber tip micro-cavity (315 pm/Mpa) [11], our TCF-based MZI shows a much higher sensitivity of −9.6 nm/Mpa and more compact structure.

Temperature response of the fiber sensor was also investigated, where the TCF-based MZI is placed into an electrical oven and gradually increasing the temperature from room temperature to 100 °C with a step of 10°C. A red shift is clearly observed when the temperature is increased. Wavelength shift of the interference dip at ~1623 nm with temperature variation is displayed in Fig. 5(d), where a good linear response with a temperature sensitivity of 43 pm/°C was obtained. The temperature response of the TCF-based MZI is mainly determined by the thermo-optical effect of the fiber core. In case no temperature compensation is employed in practical measurements, the gas pressure measurement error resulting from temperature is 4.4 KPa/°C, which is lower than the minimum detectable gas pressure change (5.2 KPa) of this MZI sensor. Hence the pressure-temperature crosstalk can be ignored.

4. Conclusions

In summary, we reported a micro-channel based TCF in-line MZI for gas pressure measurement. This device is fabricated by combining fusion splicing with fs laser micromachining technique. The two cores of the TCF perform as two interference arms and a micro-channel was drilled through one core by means of FS laser micromachining and the micro-channel worked as the precise sensing region. The proposed TCF-based MZI exhibits an ultra-high gas pressure sensitivity of −9.6 nm/MPa from 0 to 2 Mpa and a low temperature cross-sensitivity of 4.4 KPa/°C. It is suitable for gas pressure detection, biomedical sensing, environmental monitoring and other industrial applications.